PHYSICAL REVIEW B **111**, 214201 (2025)

Experimental and theoretical characterization of the prototypical Na_2S-SiS_2 electrolyte glass: Conductivity enhancement is driven by network depolymerization

M. Micoulaut,[1,*] L.-M. Poitras,[1] A. Piarristeguy,[2] O. Masson,[3,†] R. Escalier,[2] B. Ruta,[4]
V. Viallet,[5] and S. S. Sørensen[6]

[1]*Sorbonne Université, Laboratoire de Physique Théorique de la Matière Condensée, CNRS UMR 7600,*
4 Place Jussieu, 75252 Paris, Cedex 05, France
[2]*ICGM, Univ. de Montpellier, CNRS, ENSCM, Montpellier, France*
[3]*Institut de Recherche sur les Céramiques, UMR 7315 CNRS - Universit de Limoges, Centre Européen de la Céramique,*
12 rue Atlantis 87068 Limoges, Cedex, France
[4]*Institut Néel, UPR 2940, 25 Av. des Martyrs, 38042 Grenoble, France*
[5]*Laboratoire de Réactivité et Chimie des Solides, Université d'Amiens, CNRS UMR 7314, 15 Rue Baudelocque, 80000 Amiens, France*
[6]*Department of Chemistry and Bioscience, Aalborg University, Aalborg 9220, Denmark*

(Received 20 January 2025; accepted 12 May 2025; published 2 June 2025)

The structural, dynamic, and electrical properties of a prototypical amorphous electrolyte are examined using a variety of theoretical and experimental techniques. We focus on the xNa$_2$S-(100-x)SiS$_2$ system, which represents a potential application for all-solid-state batteries. First-principles molecular dynamics simulations, x-ray scattering, and conductivity experiments are performed on two select compositions of this binary: Na_2S-SiS_2 and $2Na_2S$-SiS_2. The validation of the model structures, which reproduce with excellent accuracy the measured structure functions permits examining in detail the atomic-scale picture and the effect of alkali addition. Results indicate a complete depolymerization of the network, which is characterized using the Q^n formalism, and at high Na content consists essentially of isolated $SiS_4^{4\ominus}$ tetrahedra typical of the short-range order of the corresponding crystalline compound. As in other modified chalcogenides, the simulation results reveal the presence of homopolar Si-Si and S-S defects, the latter being known to enhance ionic conductivity while the former produces isolated $(Si_2S_6)^{6\ominus}$ anions at high Na content. The measured temperature behavior of diffusivity and conductivity suggests typical Arrhenius behavior measured by complex impedance spectroscopy and not fully confirmed theoretically given the reduced *ab initio* statistics, while measured ionic conduction at room temperature is found to be similar to that of the corresponding thiogermanates. We measured an ionic conductivity of $2.9 \times 10^{-5}\ \Omega^{-1}\,\mathrm{cm}^{-1}$ at room temperature for the $2Na_2S$-SiS_2 glass.

DOI: 10.1103/PhysRevB.111.214201

I. INTRODUCTION

The development of new generations of electrochemical energy storage systems is definitely needed for carbon-free renewable energy used in vehicular propulsion, nomadic applications, and load leveling for temporal renewable energy harvesters, such as wind turbines and solar photovoltaic and solar thermal systems. Despite the current success of lithium batteries (Li ion), their dependence on flammable liquid electrolytes and on an expensive element (Li), whose natural abundance is very low, require the development of new battery systems and strategies [1–3]. Among different materials, all-solid-state batteries (ASSB) using sodium represent a promising alternative to lithium-based batteries because they are cheaper and much safer. Their standard electrode potential is comparable to that of lithium and Na is among the most abundant elements on Earth. There are still a certain number of drawbacks because ASSB is difficult to develop, and during charge and discharge processes, solid electrode/electrolyte interfaces rapidly degrade [4].

Amorphous or glassy electrolytes [5], and especially sulfides [6] represent an interesting prospect because of the possibility to alloy a nearly infinite number of components into a base material, while also displaying softer mechanical properties. This is a major advantage when compared to crystalline electrolytes, the increased polarizability of the sulfur atoms with respect to oxygen making them also more attractive. Among such sulfide glasses, the $50Na_2S$-$50SiS_2$ displays a rather limited level of conductivity [6] ($2 \times 10^{-6}\ \Omega^{-1}\,\mathrm{cm}^{-1}$), certainly smaller than the Li counterpart [7] ($10^{-4}\ \Omega^{-1}\,\mathrm{cm}^{-1}$), which has received by far more attention in early studies on amorphous electrolytes using a limited number of techniques [8–15]. Still, there is the perspective to improve the conductivity level and the glass forming ability of Na-based glasses with respect to the Li counterpart [16]. Different structural investigations (essentially spectroscopic) have been conducted in this respect [10,11,16,17], and have permitted characterization of the structure that bears similarities with archetypal sodium silicates but contains features that are specific to chalcogenides (S,Se). Scattering studies (x-ray and neutron) are limited, and we are only aware of a recent x-ray diffraction study of the $50Na_2S$-$50SiS_2$ (NS) glass [17].

---

[*] Contact author: mmi@lptmc.jussieu.fr

[†] Contact author: olivier.masson@unilim.fr

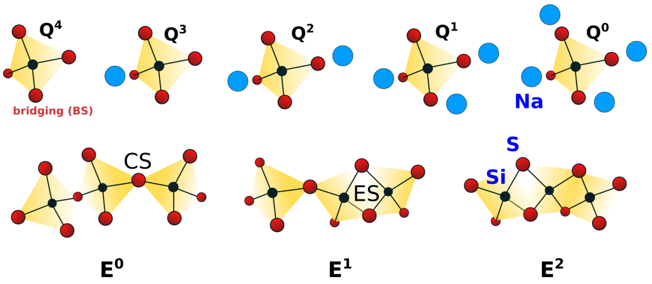

FIG. 1. Typical Q^n species found in sodium thiosilicates, ranging from Q^4 the base tetrahedra of SiS_2 to Q^0 found in crystalline orthothiosilicates [19] (Na_4SiS_4), and typical connections found in modified sulfide glasses [12]: corner-sharing (CS) and edge-sharing (ES) tetrahedra, which lead to three possible topologies: E^0, E^1, and E^2. Si, S, and Na atoms are colored in black, red, and blue, respectively.

As in silicates, the short-range order (SRO) in these modified glasses is characterized by the distribution of so-called Q^n units where n represents the number of bridging sulfur (BS) atoms connecting two Si tetrahedra together. The characterization essentially uses spectroscopic signatures such as nuclear magnetic resonance (NMR) or Raman to identify specific frequencies or chemical shifts in glasses from crystalline counterparts since the structure of the latter usually contains only a single Q^n species, e.g., 100% Q^3 in $Na_2Si_2S_5$ (33% modifier [18]) or 100% Q^0 in Na_4SiS_4 (66% modifier [19]). This leads to well-defined spectroscopic signatures, which serve to decode the spectra in glasses, and leads in most of the cases to a distribution of Q^n species (Fig. 1) [6,7,16]. The other common feature with silicates is the progressive depolymerization of the base network upon modifier addition via the creation of non-bridging sulfur (NBS) atoms having Na ions in their vicinity. As a result, the number of BS atoms decreases with increasing modifier content, and leads to a global tendency $Q^4 \rightarrow Q^3 \rightarrow Q^2 \rightarrow Q^1 \rightarrow Q^0$, and one expects a near 100% Q^0 network for extremely depolymerized glasses, which enhances ionic conduction.

In contrast to silicates, SiS_2 modified glasses display the tendency to form edge-sharing structures (Fig. 1). For instance, the structure of the sulfide counterpart of silica, SiS_2, is thought to be isomorphic [6] to the corresponding selenide glass ($SiSe_2$), which is made of infinite chains of edge-sharing (ES) tetrahedra [20]. Early NMR studies on sodium and lithium thiosilicates has shown that the spectra are essentially dominated by three resonances associated with three possible motifs or topologies [6–8,12,21]: A first one (E^0) containing no ES at all, a second one (E^1) having only a single tetrahedral edge shared, and a third one (E^2) containing two ES connections for a central tetrahedra. As for the Q^n population, the statistics of such E^k motifs evolves with modifier composition [6,16] and with the increase of network depolymerization, there is a general tendency of $E^2 \rightarrow E^1$, and $E^1 \rightarrow E^0$ conversion.

Since this glass system is important for applications as an electrolyte in ASSBs, and since it represents the sulfide counterpart of the archetypal sodium silicate, it is important to characterize in depth its properties in order to increase basic knowledge. Here, we provide a complete theoretical and experimental investigation of this sodium thiosilicate glass $x Na_2S$-$(100-x) SiS_2$ by using x-ray scattering, electrical measurements, and first-principles molecular dynamics (FPMD) simulations. The latter is found to reproduce the experimental scattering functions (pair correlation functions, structure factor) for two select compositions with excellent accuracy: $66Na_2S$-$34SiS_2$, and $50Na_2S$-$50SiS_2$. This result validates the model structures and permits full characterization of the effect of large sodium addition on structural properties, which in turn can help to establish structure-property relationships from dedicated calculated dynamic properties (diffusion, conductivity). The measured ionic conduction using complex impedance spectroscopy is found to increase with Na_2S content, and with temperature following an Arrhenius behavior. Conversely, the theoretical result is limited to the liquid state, and displays reduced statistics inherent to FPMD (small system size, short timescales), which does not fully permit concluding on a possible Arrhenius behavior. However, the nature of the Na motion can still be categorized numerically, which permits identification of immobile ions, ions with back-and-forth jumps, and ions experiencing filamentary-like motions across the (Si,S) network.

II. METHODS

A. Glass preparation

The $50Na_2S$-$50SiS_2$(NS), $60Na_2S$-$40SiS_2$(N5S3), and $66Na_2S$-$34SiS_2$(N2S) glasses were synthesized using the ball-milling technique. Stoichiometric amounts of Na_2S (Sigma-Aldrich) and SiS_2 (MSE Supplies) were first intimately mixed using a mortar and pestle. The resulting mixture was then transferred to a 20 ml tungsten carbide (WC) ball-milling jar along with 80 WC balls, each 5 mm in diameter. The total batch weight was 2.5 g, with a ball-to-powder weight ratio of 30:1. The jars were loaded into a planetary ball mill (Pulverisette 7 Premium Line, Fritsch) under an argon atmosphere, maintained inside a glove box to prevent oxidation. The synthesis process for NS and N5S3 (N2S) involved three (seven) rotation cycles, each lasting three hours, resulting in a total milling time of 9 h (21 h) at a rotational speed of 510 rpm.

B. X-ray diffraction

The atomic pair distribution functions $g_X(r)$ of the samples were obtained by x-ray total scattering. Measurements were performed at room temperature with a dedicated laboratory setup based on a Bruker D8 Advance diffractometer equipped with a silver sealed tube ($\lambda = 0.709318$ Å) and a Rapid LynxEye XE-T detector. This setup was optimized to maximize collected intensities, minimize spurious signals from the empty environment and to obtain good counting statistics up to a large scattering vector of 17.2 Å^{-1}. For both samples, a small amount of powder (around ten milligrams) was placed in a thin-walled (0.01 mm) borosilicate glass capillary of sufficiently small diameter (about 0.5 mm) to limit absorption effects. The μR values (R being the radius of the capillary and μ the linear attenuation coefficient of the sample) were estimated, using precise measurements of the mass and dimensions of the samples, to be 0.18 and 0.12 for $50Na_2S$-$50SiS_2$(NS) and $66Na_2S$-$34SiS_2$(N2S), respectively. Once sealed, the capillary was mounted on a goniometric head and adjusted so that its axis coincides with the goniometer axis of the diffractometer. The data acquisition consisted of several scans in the 0–152, 50–152, and 100–152° 2θ with a step size of 0.01°. The scans were subsequently merged, leading to a total equivalent acquisition time of about 50 hours per sample. Raw data were corrected, normalized, and Fourier transformed using homemade software [22] to obtain the reduced atomic pair distribution functions $g_X(r)$. The corrections included capillary, empty environment, Compton and multiple scatterings, absorption, and polarization effects. The x-ray mass attenuation coefficients, atomic scattering factors, and Compton scattering functions needed for data correction and normalization were calculated from tabulated data provided by the DABAX database [22,23]. The absorption correction was evaluated using a numerical midpoint integration method where the cross section of the sample is divided into a set of small subdomains following a method similar to that proposed by Soper and Egelstaf [24]. The normalization constant was determined using the high-angle method so that the coherently scattered intensity oscillates weakly around the sample's average atomic scattering factor at high values of the scattering vector length (from $k_{\max}/2$ to $k_{\max}$).

C. Conductivity

The ionic conductivity of xNa$_2$S-(100-x)SiS$_2$ glasses, with compositions of $x = 50$ (NS), $x = 60$ (N5S3), and $x = 66$ (N2S), was investigated using complex-impedance spectroscopy (CIS). Chalcogenide glass pellets, each 10 mm in diameter and weighing 120 mg, were prepared by compressing the powder under a force of five tons. The pressure was increased to 5 T over 10 min, followed by a 5-min. hold. Platinum electrodes were sputtered onto the parallel faces of the pellets to ensure electrical contact. The electrical properties of the glasses were measured using a Solartron SI-1260 impedance analyzer over a frequency range of 10 MHz to 10 Hz, with an applied root-mean-square AC voltage of 500 mV. These measurements were conducted under primary vacuum conditions at temperatures below the glass transition temperature, between 278 K and 343 K. Ionic conductivities were analyzed through Nyquist plots, where the resistance (R) of the samples was determined from the low-frequency intercept of the impedance response with the real axis. Finally, the DC conductivity was calculated using the relation $\sigma_{\rm DC} = e/RA$, where e is the thickness of the sample and A is the area of the electrode surface.

D. Molecular dynamics

FPMD simulations (Car-Parrinello scheme [25]) have been performed on the two compositions NS and N2S within a canonical (NVT) ensemble using the density functional theory (DFT-D2) scheme, which incorporates a dispersion (van der Waals) correction [26]. The simulation box contained $N = 300$ atoms with the number of Si, S, and Na atoms fulfilling the desired stoichiometry, i.e., $N_{\rm S} = N_{\rm Na} = 132$ and $N_{\rm Si} = 36$ for N2S, and $N_{\rm S} = 150$, $N_{\rm Na} = 100$, and $N_{\rm Si} = 50$ for NS. A periodically repeated cubic cell was used, with edges L satisfying the experimental number density of the corresponding glasses [16], i.e., $L = 19.098$ Å and 19.113 Å for NS, and N2S, respectively. We used DFT in combination with plane-wave basis sets, the electronic scheme being based on a BLYP functional [27,28] within GGA for the exchange-correlation energy. The choice of this functional is motivated by the fact that previous investigations of base networks have led to a very accurate structural description of the amorphous state [29–32] including sulfide glasses [33,34]. The electronic structure of the liquids and glasses was described within DFT and evolved self-consistently during the motion, with valence electrons being treated explicitly in conjunction with norm-conserving pseudopotentials to account for core-valence interactions. The wave functions were expanded at the Γ point of the supercell and the energy cutoff was set at 80 Ry.

The starting configuration of the N2S glass was taken from a previous 66Na$_2$S-34GeS$_2$ system [35] and appropriately rescaled in order to meet the desired number density. The other configuration (NS) was obtained from a random substitution of atoms of the N2S. Loss of memory of the initial configurations has been achieved through preliminary runs at 2000 K over 20 ps with a time step of $\Delta t = 0.12$ fs and a fictitious mass of 2000 a.u., before different equilibrations at 1500 K, 1200 K, 900 K, and 600 K, each accumulated over 20–30 ps, and finally 300 K for 30 ps. The cooling procedure was performed sequentially, e.g., the equilibration at 900 K started from the last configuration (positions/velocities) obtained at 1200 K, and so on. The presented results at 300 K are obtained from a statistical average over $\simeq$20 ps once the first 5 ps have been discarded.

III. STRUCTURAL PROPERTIES

A. Scattering functions in reciprocal space

Figure 2(a) represents the calculated and measured x-ray structure factors, denoted $S_X(k)$ hereafter. Here, we have used for the calculated function weighted sums of partial correlations $S_{nm}(k)$ in Fourier space,

$$S_X(k) = \langle f\rangle^{-2}\sum_{n,m} c_n c_m f_n f_m S_{nm}(k) \tag{1}$$

with

$$\langle f\rangle = \sum_n c_n f_n = (1-x)f_{\rm Si} + 2x f_{\rm Na} + (2-x)f_{\rm S}, \tag{2}$$

where c_n represents the species concentration. For the coefficients f_n, we have used atomic form factors taken as $f_n = Z_n$ ($f_{\rm Si} = 14$, $f_{\rm S} = 16$, $f_{\rm Na} = 11$). Note that a k dependence of the form factors did not lead to significant differences. For NS, this leads to

$$S_X(k) = 0.028\,S_{\rm SiSi} + 0.190\,S_{\rm SiS} + 0.087\,S_{\rm SiNa} + 0.327\,S_{\rm SS} + 0.299\,S_{\rm NaS} + 0.069\,S_{\rm NaNa}, \tag{3}$$

and for N2S, one has

$$S_X(k) = 0.014\,S_{\rm SiSi} + 0.123\,S_{\rm SiS} + 0.083\,S_{\rm SiNa} + 0.277\,S_{\rm SS} + 0.375\,S_{\rm NaS} + 0.127\,S_{\rm NaNa}. \tag{4}$$

The partial correlations appearing in Eq. (1) have been evaluated from a Fourier transform of the partial pair correlation functions $g_{nm}(r)$,

$$S_{nm}(k) = 1 + \rho_0 \int 4\pi r^2[g_{nm}(r) - 1]\frac{\sin(kr)}{kr}dr, \tag{5}$$

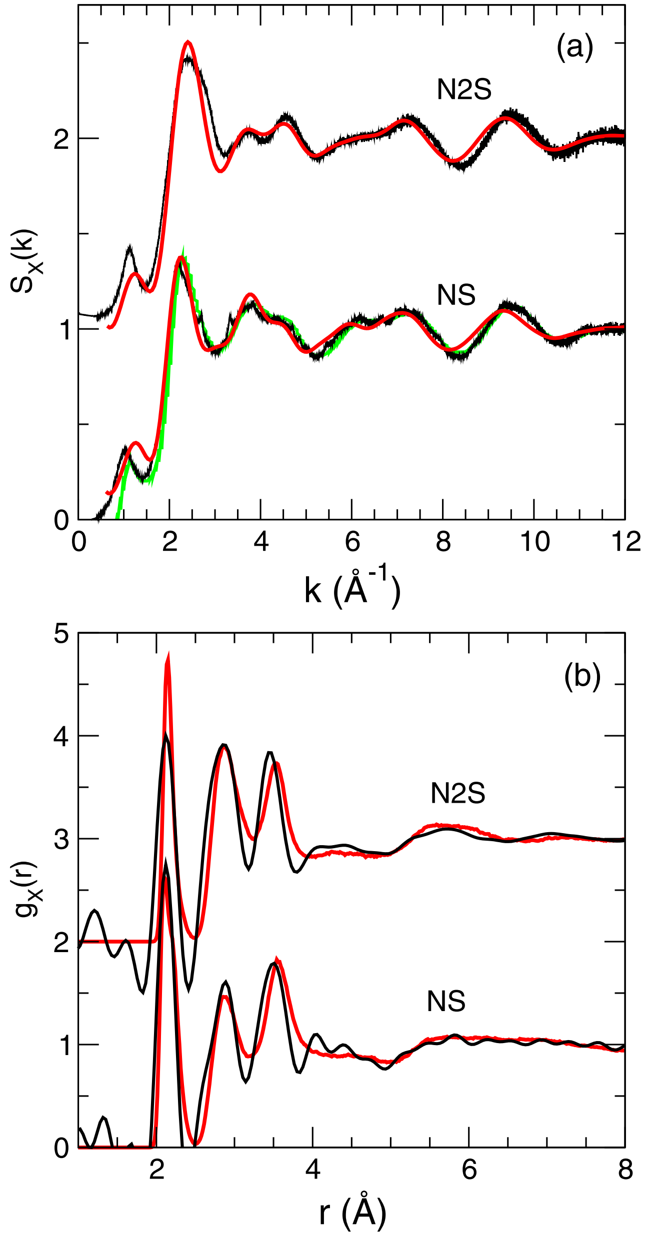

FIG. 2. Calculated (red) and measured (black) x-ray-weighted total structure factor $S_X(k)$ (a) and pair-correlation functions $g_X(r)$ (b) for NS and N2S glasses. In addition, XRD data from Dive *et al.* [17] (NS composition, green) have been added. For clarity, vertical shifts of +1 and +2 are added in (a) and (b) for the N2S glass, respectively.

where ρ_0 is the system number density $\rho_0 = 0.0431$ Å^{-3} and $\rho_0 = 0.0429$ Å^{-3} for NS and N2S, respectively. These are linked with the cell sizes provided above.

1. Theory versus experiment

The comparison between the calculated and measured $S_X(k)$ (red and black curves, respectively) is shown in Fig. 2(a), and suggests an excellent agreement between simulations and experiment; the level of agreement being of the same order as previously obtained for germanium based sulfides [35]. We note that all principal peaks (PP) are reproduced in position, amplitude including in the low k region corresponding to the first sharp diffraction peak (FSDP) observed at 1.15 Å^{-1} and 1.04 Å^{-1} for N2S and NS, respectively. The simulation here underestimates slightly the position with the corresponding experimental values found at 1.29 and 1.26 Å^{-1}. In both simulations and experiments, the diffraction pattern is dominated by three peaks found at $k_1 = k_{\rm FSDP} \simeq 1.05$ Å^{-1}, $k_2 \simeq 2.3$–2.5 Å^{-1} and in the region $k_3 \simeq 4.0$ Å^{-1}. We remark that the increase of Na content (i.e., from NS to N2S) induces an increase of k_2 (from 2.26 to 2.46 Å^{-1}) and also a reduction of the peak at 4.0 Å^{-1} at the expense of another peak at 4.5 Å^{-1}. An inspection of the details of the partial structure factors indicates that emerging Na-S and Na-Na correlations are responsible for this trend (Fig. 3).

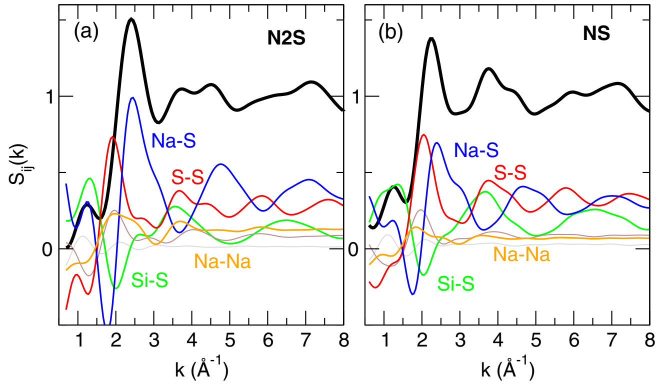

FIG. 3. Decomposition of weighted partials $\langle f\rangle^2 x_i x_j f_i f_j S_{ij}(k)$ in N2S (a) and NS (b) glasses. The black-thick line is the calculated total x-ray structure factor [same as Fig. 2(a)]. Only the relevant partials are marked.

We furthermore note that the peaks beyond the PP region are also correctly reproduced. A Gaussian decomposition of $S(k)$ has shown that such peaks ($k \simeq 6$–7 Å^{-1}) result from well-defined second-neighbor correlations [36].

Using the simulation results, a decomposition of the total structure factors into relevant partials $S_{ij}(k)$ suggests indeed that the N2S glass has two dominant contributions to the PP at k_2: Na–S and S–S [Fig. 3(a)]. Concerning the latter, we note that the reduction of the amplitude of the corresponding partial $S_{\rm SS}(k)$ in the region of $k_3 \simeq 4.0$ Å^{-1} is responsible for the change in profile of the double peak located at 3.8 and 4.4 Å^{-1}, which evolves from a distribution dominated by the low k peak [NS, Fig. 3(b)] to a more balanced distribution at elevated modifier content [Fig. 3(b)]. Finally, the other important partials contributing to the total $S(k)$ are the Si-S partial and the Na-Na partial, which has an increased contribution at low k ($k_0 \simeq 2.0$–2.5 Å^{-1}) for the N2S glass, indicative of the emergence of a corresponding length scale of about $7.7/k_0 \simeq 3.1$–3.8 Å. All other partials (Si–Si, Si–Na, brown and gray curves, respectively) have a contribution [see Eqs. (3) and (4)] that is less than 10%.

2. Theory versus theory

A previous DFT-based molecular dynamics simulation has been performed [17] on the NS glass, together with an experimental x-ray scattering measurement. While the latter is fully compatible with our present XRD results [green curve

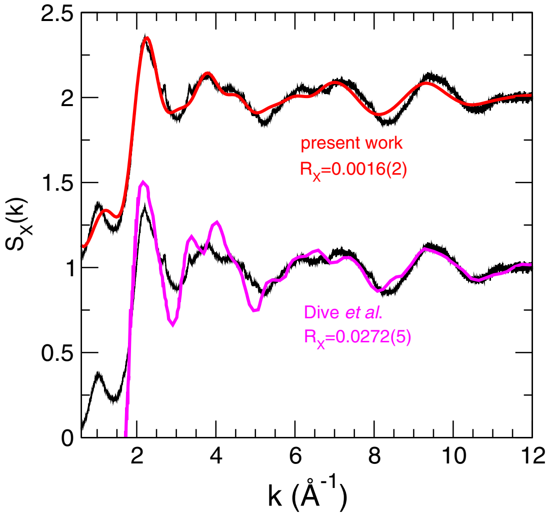

FIG. 4. Comparison between the present DFT-BLYP scheme (red) and a previous DFT-PBE calculation from Dive *et al.* [17] (magenta) on the NS glass. The black curve corresponds to the present experimental XRD measurement, and has been duplicated.

in Fig. 2(a)], we note that the former differs substantially from our results (Fig. 4), and is unable to reproduce a certain number of features of the structure factor: absence of the FSDP, fair reproduction of the PP at k_2, poor reproduction of the PP at k_3. In this respect, the present simulations provide a clear step forward in the successful modeling of NS atomic structures.

The calculation of a goodness-of-fit (Wright) parameter [37], which builds on a least-squares comparison between simulation and experimental data, provides some quantitative information on the level of agreement,

$$R_X = \left(\frac{\sum_i [S_{\rm exp}(k_i) - S_{\rm calc}(k_i)]^2}{\sum_i S^2_{\rm exp}(k_i)} \right)^{1/2}. \qquad (6)$$

When we compare $S_{\rm calc}$ and $S_{\rm exp}$ in the range $0.6\ \text{Å}^{-1} \leqslant k \leqslant 12.0\ \text{Å}^{-1}$ for both simulations, we find $R_X = 0.0016(2)$ for our present simulation and a substantially higher value for the DFT simulation of Dive *et al.* [17], which was $R_X = 0.0272(5)$. In addition, the spurious effects observed at intermediate and large k result in an incorrect second- and third-shell correlation of neighbors expected at 2.89 Å and 3.50 Å.

While the system size might affect the overall results and especially the low-k region (300 atoms vs 144 atoms [17]) as reported in certain methodological studies [38,39], we first note that both systems have been simulated at the same density ($2.0\,\mathrm{g\,cm^{-3}}$) and with a nearly similar thermal history ($10\,\mathrm{K\,ps^{-1}}$ vs $10^2\,\mathrm{K\,ps^{-1}}$), except for the randomization of the initial configuration that we have performed over much longer simulation times (20 ps vs 0.1 ps). Actually, the major difference between the two simulations relies on the choice of the exchange correlation functional (BLYP in the present case versus Perdew-Burke-Ernzerhof (PBE) [17]). Previous investigations on chalcogenide glasses and especially network formers (GeS_2, $GeSe_2$) have suggested that the full account of the structural features depends on subtle effects involved in the electronic modeling of the chemical bonding, from covalent to ionic [40]. For instance, it has been shown that PBE leads to a slight overestimation of the metallic character of the bonding [29] that induces a certain number of flaws in structural properties for both the liquid and the amorphous phase [30]: increase of coordination defects and reduction of tetrahedral character, reduction of the FSDP that can even vanish in certain select DFT models [34,41]. Such flaws are reduced once a BLYP functional is used. We finally remark that the other major difference between both models is the use of a van der Waals correction, which is absent in the study of Ref. [17]. It might be interesting to probe different DFT models in a systematic way as those carefully performed, e.g., tellurides [42,43], but this is not the purpose of the present study.

B. Real-space properties

The total pair-correlation functions $g_X(r)$ accessed from XRD are displayed in Fig. 2, together with the corresponding simulation results (red curves). An excellent agreement is obtained for both compositions and leads to reproduction in terms of position, intensity, and width of the PPs in NS and N2S. Specifically, we find the PP at 2.11 Å and secondary peaks at 2.90 Å and 3.5 Å, all being weakly sensitive to composition albeit an obvious increase of the first secondary peak is acknowledged with increasing Na_2S content. The origin of these different contributions can be decoded from the partial correlation analysis as discussed next.

1. Presence of Si–Si homopolar bonds

Figure 5 represents the different pair-correlation functions $g_{ij}(r)$ of the NS and N2S glasses. We first concentrate on the Si–Si partial $g_{\rm SiSi}(r)$, which displays a three-peak structure that is typical of chalcogenides [44,45]. The first peak at 2.37 Å is usually associated with homopolar bonds, and an inspection of the atomic snapshots permits us, indeed, to relate this distance with the Si–Si bond length. A second peak at $r \simeq 3.0$ Å is only present for the NS composition and is related with the presence of ES motifs [45], as also found in different sulfide and selenide glasses [33,34,44,46]. As such motifs tend to disappear upon network depolymerization [6] and reduction of the number of BS atoms, it is not particularly surprising that this ES signature is absent in a glass with a large amount of modifier (N2S). Finally, a third peak is clearly observed at $r \simeq 3.62$ Å for the NS composition, and shifts to 3.82 Å for N2S, in agreement with an overall increase of the Si–S–Si bond angle (see below). This peak obviously narrows with modifier content, and has a mixed origin. At moderate depolymerization, the distance that is very well analyzed in the literature [33,44,45] is associated with the presence of CS connections between tetrahedra via a BS atom, whereas at elevated modifier content (i.e., N2S), it is essentially linked with a correlation distance between separated Si atoms belonging to Q^0 units.

The existence of a homopolar Si–Si bond might be regarded as surprising given its complete absence in the sodium silicate analog. However, in contrast to the latter a crystalline sulfide phase ($Na_6Si_2S_6$) has been identified [47,48], and is

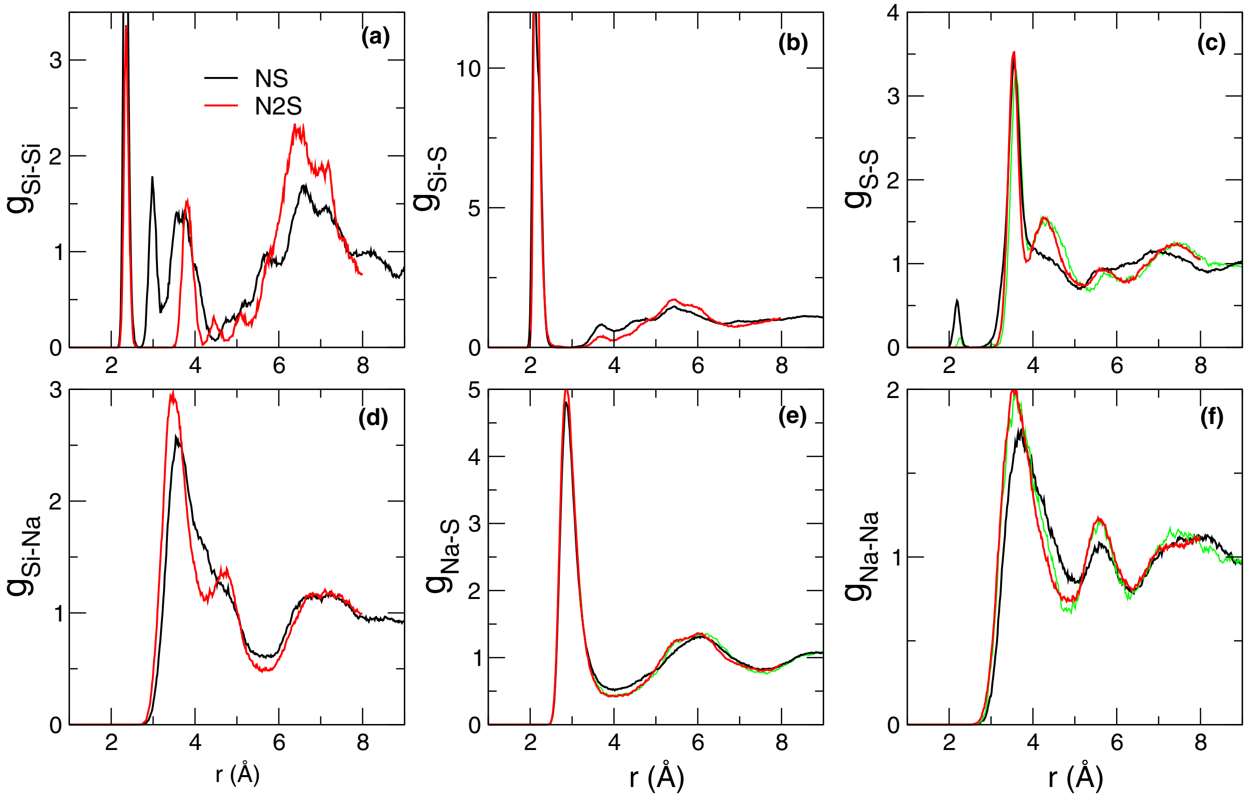

FIG. 5. Partial pair-correlation functions $g_{ij}(r)$ of NS (black) and N2S (red). Corresponding partials of N2G (66Na_2S-34GeS_2) are provided (green [35]).

found to display a Si–Si homopolar bond rather than the usual Si–S–Si one involving a BS atom. In the glass, the presence of this short range motif (an ethane-like structure having 6 NBS atoms) that is obtained from the simulation and manifests as the peak at 2.37 Å in $g_{\mathrm{SiSi}}(r)$ might be driven by the similar short-range order of the corresponding crystalline phase formed in the range of composition that we have targeted numerically ($50 \leqslant x \leqslant 66\%$). This motif is actually confirmed from a spectroscopic (NMR) signature [16] and has a specific signature in the same range $50\% \leqslant x \leqslant 66\%$ for corresponding glasses. The presence of such homopolar bonds is not restricted to the present sodium thiosilicate since previous investigations have suggested the presence of Ge-Ge bonds in Na_2S-GeS_2 glasses [35] and there is also clear evidence of P-P bonds in amorphous thiophosphates [49–51].

The presence of such ethane-like units involves a higher proportion of S–S bonds that can be translated through a partial disproportionation reaction of the network species, $SiS_2 \rightarrow SiS + S$, leading to the formation of additional sulfur. For the composition at which the effects of the network former are still present (NS), the presence of such homopolar S–S bonds is acknowledged in Fig. 5(c), and corresponds to the prepeak obtained at 2.20 Å that is a value typical of network chalcogenides (2.11 Å) such as in GeS_2 [33] or GeS_4 [32]. The presence of such homopolar sulfur or "isolated sulfur" [52] is thought to achieve extended and interconnected pathways promoting conduction. Finally, regarding the S–S partial, we find that the PP is associated with the edge of the $SiS_{4/2}$ tetrahedra (3.55 Å), whereas the secondary peak only visible for N2S is linked with correlations between sulfur of different tetrahedra that have been isolated by the disruption of BS atoms.

Taken together, the evolution of the pair correlation functions [and especially $g_{\mathrm{SiSi}}(r)$] suggests a profound alteration of the network structure with modifier content.

2. *Other partials*

The other calculated partials turn out to be weakly sensitive to composition. This is particularly obvious for Si-S [Fig. 5(b)] and Na-S correlations [Fig. 5(e)], displaying almost no changes, which indicates that the elementary SRO and the apex defining the $SiS_{4/2}$ tetrahedra remain unchanged, whereas the typical bonding correlations between sodium and NBS atoms are not affected by the addition of additional Na_2S. These conclusions hold to a lesser extent for the partials Si-Na, and Na-Na, the latter displaying for the N2S composition, furthermore a similar profile as the isochemical N2G (66Na_2S-34GeS_2) glass [35]. We find corresponding bond lengths $r_{\mathrm{Si-S}} = 2.15$ Å (Table I) and $r_{\mathrm{Na-S}} = 2.85$–2.86 Å, the former being consistent with the present experimental findings since the PP of the total pair-correlation function $g_X(r)$ [Fig. 2(b)] corresponds to the Si–S distance found at 2.15(2) Å for both compositions.

3. *Coordination numbers*

We focus on the SRO characteristics and especially on partial- and species-related coordination numbers, n_{ij} and n_i,

TABLE I. Typical bond distances r_{ij} (in Å) and coordination numbers n_{ij} of network species calculated from the relevant partials in NS and N2S glasses. A second line is written for partials displaying several peaks at distances corresponding to the first coordination shell.

	Si–Si		Si–S		S–S		Na–S	
	r_{ij}	n_{ij}	r_{ij}	n_{ij}	r_{ij}	n_{ij}	r_{ij}	n_{ij}
NS	2.37	0.39	2.15	3.59	2.20	0.10	2.86	6.66
	3.00				3.55			
N2S	2.37	0.16	2.15	3.74			2.85	5.88
					3.55			

which are extracted from the relevant partials according to

$$n_{ij} = 4\pi\rho_0 \int_0^{r_{\rm min}^{ij}} r^2 g_{ij}(r)dr \tag{7}$$

and

$$n_i = n_{ii} + \sum_{j\neq i} n_{ij}, \tag{8}$$

where $g_{ij}(r)$ are the partial pair-correlation functions given in Fig. 5, and ρ_0 are the densities of the NS and N2S glasses. One furthermore has the property $N_i n_{ij} = N_j n_{ji}$, where N_j represent the number of atoms of type j in the system. The values $r_{\rm min}^{ij}$ have been all taken at the minimum of the corresponding $g_{ij}(r)$ function, e.g., $r_{\rm min}^{ij} = 4.02$ Å for Na-S. Corresponding data (n_{ij}) can be found in Table I for the network species (Si,S). These indicate that the Si coordination number is equal to $n_{\rm Si} = 3.98$ and 3.90 for NS and N2S, respectively, and result from contributions arising from Si–S and the ethane-like structure having a Si–Si bond, whose concentration is provided below.

Concerning the sulfur coordination, it results mostly from S–Si and S–Na correlations (and a minor contribution from homopolar S–S bonds in NS). We found for both compositions a coordination number that is fully compatible with the octet rule, i.e., $n_S = 2.04$ and 2.16 for NS and N2S glass (Table II), respectively. Finally, the sodium coordination number is found to be larger than 5 as in a number of Na-based modified glasses such as silicates [53,54] or (thio)germanates [35,55]; the difficulty [56] being to estimate correctly n_{ij} from Eq. (7) for species that do not display a global minimum in the corresponding pair correlation function, i.e., $g_{ij}(r_{\rm min}^{ij}) \neq 0$. Figure 6(a) represents the Na-related pair correlation function defined by

$$g_{\rm Na}(r) = \sum_i c_i g_{i{\rm Na}}(r), \tag{9}$$

which displays for both compositions only a local minimum at $r_{\rm min}^{\rm Na}$ used for the calculation of $n_{\rm Na}$ (e.g., 3.23 Å for N2S). As a result, the running coordination number $n_{\rm Na}(r)$ does not display a plateau value $n_{\rm Na}$ = Cst as for network species [Fig. 6(b)]. Using the corresponding minima $r_{\rm min}^{\rm Na}$ [see numbers in Fig. 6(a)], we find $n_{\rm Na} = 5.68$ and 5.05 for NS and N2S, respectively. This is somewhat expected since Na is sixfold coordinated in the corresponding crystalline compounds [18,57]. In order to provide additional information on the sodium environment, we have considered the distribution of Na neighbors with increasing distances. This leads to neighbor-distribution functions NDF$_j(r)$ for an arbitrary number N of neighbors ($1 \leqslant j \leqslant N$), as exemplified in different liquids and glasses [36,58,59]. For each atom, these NDFs are constructed by sorting the neighbors according to the bond length. Figure 6(c) now represents these NDFs for up to $N = 10$ neighbors. We first remark that the composition weakly impacts the neighbors of Na, as both calculations for NS and N2S lead to the same pattern of NDFs, and this is especially true in the first coordination shell when $r \leqslant r_{\rm min}^{\rm Na}$. The second outcome is the presence of a smooth increase of the average sodium neighboring distance [inset of Fig. 6(c)], and differences between NS and N2S are barely visible, except at large j (second or third coordination shell). This suggests that although the network is continuously depolymerized between NS and N2S, the topology of the underlying Na subnetwork is not dramatically modified. In corresponding oxides, molecular simulations suggest [53,60] that this Na subnetwork has an inhomogeneous structure with the presence of Na clustering or preferential pathways for ion motion [61,62] (channels). Descriptors usually focus on the intensity of the Na-Na pair correlation function [60] or on the prepeak in quasi-elastic neutron scattering patterns [63,64], as also examined from the partial Na-Na structure factor $S_{\rm NaNa}(k)$. Both Figs. 3 and 5(f) indicate a weak dependence of such descriptors with composition, $g_{\rm NaNa}$ and $S_{\rm NaNa}$, albeit the intensity of the principal peak of the former is found to increase with modifier composition that is sometimes interpreted [60] as clustering. A visual inspection of the atomic simulation boxes suggests that on longer ranges (i.e., beyond the neighbor rank 8–9, Fig. 6), the spatial distribution of Na atoms undergoes obvious changes, as discussed below.

TABLE II. Calculated coordination numbers n_i (i = Si, S, Na) in NS and N2S glasses. A cut-off $r_{\rm min} = 2.8$ Å {(minimum of $g_i(r)$] has been used for the network species, whereas $r_{\rm min} = 3.32$ Å and 3.23 Å for Na in NS and N2S, respectively (see text for details).

System	$n_{\rm Si}$	n_S	$n_{\rm Na}$
NS	3.98	2.04	5.68
N2S	3.90	2.16	5.05
N2G [35]	3.84	1.90	5.82

4. Q^n speciation

An additional structural analysis builds on the Q^n terminology (Fig. 1) that we determine from the obtained model structures by enumerating for each configuration the number of Si displaying the sequence Si–S–Na within a fixed cut-of at 4.2 Å [minimum of the partial $g_{\text{Si-Na}}(r)$]. The calculated Q^n distribution of the simulated NS and N2S glasses is provided in Table III, and compared to the experimental determination from NMR [16]. Here, we first note that for both compositions, as in experiments [16], there are ethane-like (Eth) structures containing a homopolar bond that contribute to $Na_6Si_2S_6$ species. In xNa$_2$S-(100-x)SiS$_2$ glasses, NMR finds

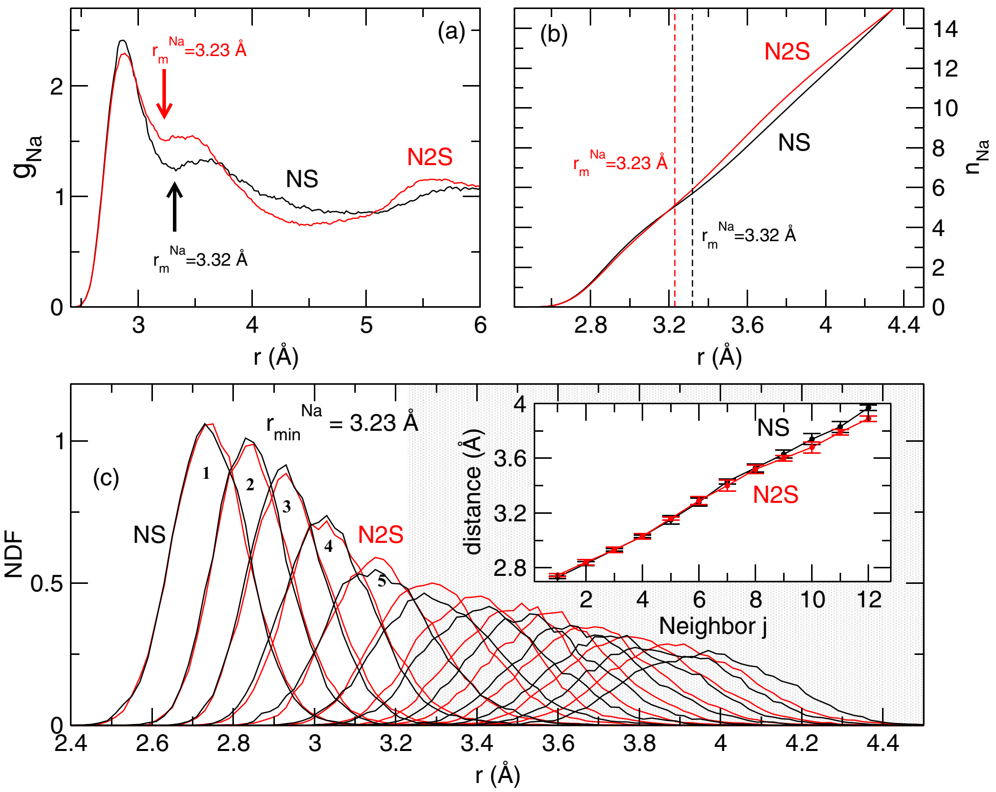

FIG. 6. (a) Calculated Na-based pair correlation function in NS (black) and N2S (red) glasses. The arrows indicate the positions $r_{\rm min}^{\rm Na}$ of the (local) minimum. (b) Corresponding running coordination number $n_{\rm Na}(r)$. (c) Neighbor distributions NDF$_k(r)$. The gray zone corresponds to the approximate region of second shell neighbors at $r > r_{\rm min}^{\rm Na}$. The inset shows the maximum of each distribution NDF$_k(r)$ with neighbor number k.

such molecules in the range $55\% \leqslant x \leqslant 60\%$ with a fraction of about 10%. Noteworthy is the fact that such chemical defects are highly sensitive to thermal history effects [65,66] so that we can only stress that their presence in the DFT models is qualitatively compatible with the tendency to have such molecules in depolymerized thiosilicates.

The other species cover as in classical MD studies a broad Q^n distribution that shifts to higher n with increasing modifier content. For the NS glass, we predominantly find Q^2 species that are expected to maximize on the basis of a simple stoichiometric (chemical) argument, and here they represent 47.6% of Si atoms, slightly lower than the measured NMR population [16]. One thus expects to still have the possibility of ES connections, as at least two BS atoms are needed to form such ring structures. These are indeed detected from atomic snapshots (Fig. 7, right) and lead to a dedicated peak in the Si-Si partial [Fig. 5(a)] as previously discussed. The other dominant population in NS glasses is represented by Q^1 units (10.3% to be compared with the experimental 22.0%), which grow dramatically for higher modifier concentrations (N2S) and then represents 40.2% of all Si atoms. At this composition of $x = 66\%$, the network is almost entirely depolymerized (Fig. 7, left) and the structure is made of Q^1–Q^1 dimers ($Na_6Si_2S_7$), ethane-like molecules ($Na_6Si_2S_6$) and isolated Q^0

TABLE III. Calculated fraction (in %) of Q^n distribution and ethane-like unit (Eth) in NS and N2S glasses, and compared to the NMR determination from Watson *et al.* [16] and to basic (chemical ordered) models. LS corresponds to the lithium isochemical compound [67] (50 Li_2S-50 SiS_2).

	Eth	Q^4	Q^3	Q^2	Q^1	Q^0
NS	34.0		4.0	47.6	10.3	4.1
NMR [16]				64.0	22.0	
Chemical ordered model				100.0		
LS [67]		5.8	20.7	35.4	30.6	7.5
Topological model [68]		8.6	19.2	35.2	36.8	
N2S	15.6			2.8	40.2	41.2
NMR [16]					24.0	76.0
Chemical ordered model						100.0

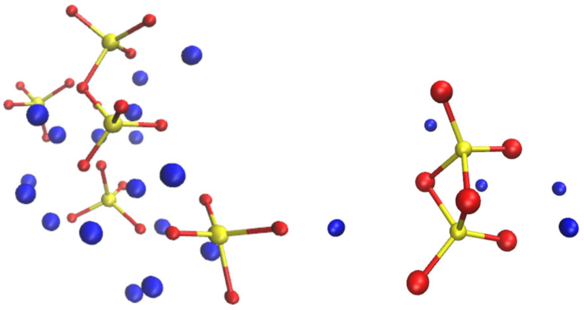

FIG. 7. (Left) Snapshot of a N2S structural fragment highlighting the network depolymerization. (Right) ES tetrahedra in NS.

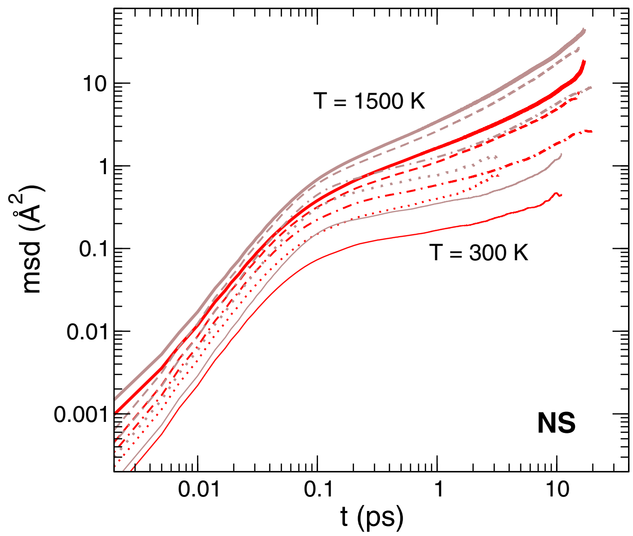

FIG. 8. Calculated mean-square displacement $\langle r_k^2(t)\rangle$ for $k =$ Na (brown), and $k =$ S (red) (Si behaves almost like S) with time for different isotherms in liquid NS: 1500 K (thick solid), 1200 K (broken), 900 K (dashed-dotted), 600 K (dotted), 300 K (thin solid).

species (Na_4SiS_4), the latter having a probability of 41.2%, i.e., lower than the value (76.0%) measured from NMR [16].

It is important to emphasize that in contrast to oxide glasses [69], the Q^n population is difficult to establish from NMR owing to the small number of reference crystalline phases ($Na_2Si_2S_5$ [18], Na_2Si_3 [6], and $Na_2Si_2S_5$ [19]). This is a major difference with, e.g., sodium silicates for which numerous phases serve for the NMR chemical shift identification. Secondly, the small ^{29}Si chemical shift anisotropies in thiosilicates lead to obvious uncertainties, which do not permit always distinguishing between various Q^n species [6] and their evolution with composition. Finally, we note that the alkali type and thermal history [70] both affect the Q^n distribution as highlighted by a previous estimate for lithium thiosilicates (LS [67]) obtained from a classical force-field, and which displays a broad distribution covering all n values, whereas NMR results suggest a binary model predominantly made of Q^4 (the base short-range order of SiS_2) and Q^2 species [12].

IV. DYNAMICS

Since these sodium thiosilicate systems are thought to be used in fast ion solid state batteries, it is instructive to infer some transport properties in relationship with structure.

Diffusivity

We first focus theoretically on the dynamics of the NS and N2S melts by focusing on the mean-square displacement (msd) of the atoms, defined from the positions $\mathbf{r}_j(t)$ at time t

$$\langle r_k^2(t)\rangle = \left\langle \frac{1}{N_k}\sum_{j=1}^{N_k} |\mathbf{r}_j(t) - \mathbf{r}_j(0)|^2 \right\rangle, \tag{10}$$

where the sum is taken over all atoms of type k ($k =$ Si, S, Na).

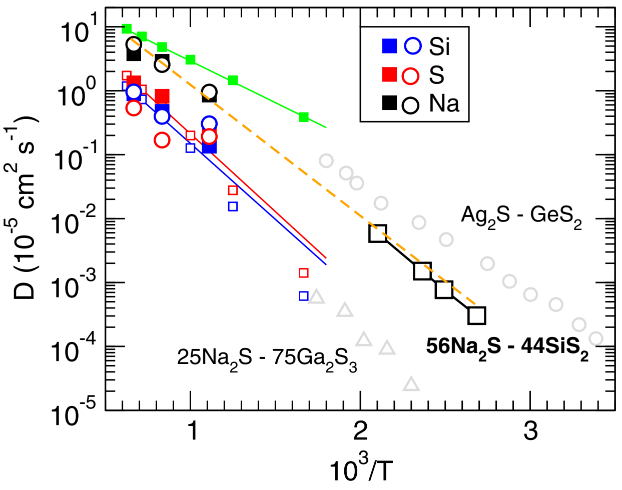

FIG. 9. Calculated diffusivity D_k with $k =$ Si (blue), S (red), and Na (black) in molten NS (filled squares) and N2S (open circles). These data are compared to calculated diffusivities [71] from a classical force field [small green symbols for Na, otherwise red (S) and blue (Si)], and to experimentally measured Na diffusivities [72] in $56Na_2S$-$44SiS_2$ (open squares). Data on other chalcogenides [73,74] are also represented for comparison (gray open symbols). The orange-broken line serves as a guide to highlight the compatibility of the DFT data with experiment.

Figure 8 represents $\langle r_k^2(t)\rangle$ for the NS composition and for two select species (Na, S) at the different considered isotherms. An inspection of the time dependence signals that the diffusive regime is obtained at high temperature (1500 K, 1200 K, and 900 K) within the simulation time, whereas a dynamic slowing down is acknowledged for the lower temperatures (600 K and 300 K), and prevents estimating corresponding diffusivities.

The self-diffusion constant D_k in the long-time limit is defined from the Einstein equation

$$D_k = \frac{1}{6}\lim_{t\to\infty}\frac{d\langle r_k^2(t)\rangle}{dt}. \tag{11}$$

Diffusivity results are displayed in Fig. 9 in an Arrhenius representation for both NS (filled squares) and N2S (open circles) liquids. Here, the semi-log representation as a function of inverse temperature usually reveals the dynamics of activated (Arrhenius) type. Corresponding numbers are provided in Table IV. Note that we have limited the study to high-temperature melts since we need a clear diffusive regime at long time to safely establish the diffusivity from Eq. (11). For the standard DFT simulation time achieved at fixed T ($\simeq$20 ps), this limits the investigation to the range $900\,\text{K} \leqslant T \leqslant 1500$ K. Given the limited number of data points, it is not clear if the diffusivities follow an Arrhenius behavior $D \propto \exp[-E_A/k_BT]$. While this might be the case for the Na ions (with an estimated activation energy $E_A = 0.35$ eV for both NS and N2S), the trend for the network species appears to be not conclusive. The value E_A is somewhat higher than the one previously determined from classical molecular dynamics simulations (0.25 eV from $D_{Na}(T)$ [71]) but the latter have been found to poorly reproduce the structural properties, and

TABLE IV. Calculated diffusivities D_i ($i = \text{Si, S, Na}$) in 10^{-5} cm^2 s^{-1} in molten NS and N2S systems. See also Fig. 9.

		D_{Si}	D_{S}	D_{Na}
NS				
	1500 K	0.90 ± 0.02	1.33 ± 0.02	3.80 ± 0.06
	1200 K	0.47 ± 0.02	0.82 ± 0.02	2.88 ± 0.03
	900 K	0.14 ± 0.02	0.27 ± 0.05	0.85 ± 0.07
N2S				
	1500 K	0.54 ± 0.03	0.96 ± 0.03	5.33 ± 0.06
	1200 K	0.17 ± 0.02	0.40 ± 0.03	2.57 ± 0.05
	900 K	0.19 ± 0.02	0.31 ± 0.02	0.95 ± 0.02

have led to diffusivities slightly larger (small green symbols, Fig. 9) than the present *ab initio* results.

The present calculated Na diffusivities are compatible with data determined at low temperature by Thomas *et al.* from ^{22}Na tracer diffusion experiment [72] on a slightly different composition (56Na$_2$S-44SiS$_2$) with a Na activation energy $\text{E}_A = 0.44$ eV. The compatibility of the data does not necessarily mean that our liquid data could extrapolate down to the glassy state given that the Na dynamics is supposed to be dramatically modified across the glass transition region, but the data compatibility simply signals that the electronic model is accurate enough to provide realistic diffusivities. In addition, we point out that the obtained values are also of the same order as those measured in similar modified sulfide glasses [73,74]. We, furthermore, note a meaningful difference between ion and network dynamics, which emerges as the temperature is lowered, and D_{Si} and D_{S} are found to be systematically lower than D_{Na} by a factor of about 6–8 in the temperature range of interest. This diffusivity difference is supposed to increase [75] as the temperature continues to decrease. In the glassy state, the resulting Na diffusivity is, therefore, strongly decoupled from the Si and S diffusivities, and this corresponds to the usual picture of an amorphous electrolyte displaying a significant Na mobility in a frozen (Si,S) disordered matrix.

The second melt (N2S) is found to display diffusivities that are not substantially different from those determined for NS as we find, e.g., for 900 K $D_{\text{Na}} = 0.85 \pm 0.17 \times 10^{-5}$ cm^2 s^{-1} to be compared with $0.95 \pm 0.02 \times 10^{-5}$ cm^2 s^{-1} for N2S at the same temperature (Table IV). This is probably linked with the fact that the underlying structure of the Na subnetwork is not radically different as revealed from the neighbor distribution functions [Fig. 6(c)], although the spatial distribution for the Na motion is slightly different at long range (Fig. 6), as discussed below.

V. CONDUCTIVITY

A. From the MD simulations

The conductivity (σ) as a function of temperature T can be obtained from the Green-Kubo equation [76],

$$\sigma(T) = \lim_{t\to\infty} \frac{Ne^2}{6tVk_BT} \sum_{i,j} z_i z_j \langle [\mathbf{r}_i(t) - \mathbf{r}_i(0)][\mathbf{r}_j(t) - \mathbf{r}_j(0)] \rangle, \tag{12}$$

where V is the volume of the simulation box, e is the elementary charge, z_i and z_j are the nominal charges of ions i and j, respectively (+4, –2, and +1 for Si, S, and Na, respectively). Here, $\mathbf{r}_i(t)$ is the position of atom i, and the brackets $\langle\rangle$ denote ensemble averages.

An alternative means is provided by linear response theory using the current autocorrelation (AF) function,

$$\sigma(T) = \frac{e^2}{Vk_\text{B}T} \int_0^\infty \sum_{i,j} z_i z_j \langle \mathbf{v}_i(0) \cdot \mathbf{v}_j(t) \rangle \mathrm{d}t, \tag{13}$$

which can be split into self- and cross-parts, yielding

$$\sigma(T) = \frac{e^2}{Vk_\text{B}T} \int_0^\infty \sum_i z_i^2 \langle \mathbf{v}_i(0) \cdot \mathbf{v}_i(t) \rangle \mathrm{d}t + \frac{e^2}{Vk_\text{B}T} \int_0^\infty \sum_{i,j,i\neq j} z_i z_j \langle \mathbf{v}_j(0) \cdot \mathbf{v}_i(t) \rangle \mathrm{d}t. \tag{14}$$

Here, the first term is the self-part and can be directly related [76] to the self-diffusion coefficients D_k, whereas the second term corresponds to the cross-correlations between different atoms. The cross (or distinct) term involves a double summation with $N(N-1)$ operations. Practically, the cross terms require significantly more statistical averaging than the autocorrelation terms [77]. As a result, given the reduced system size and the limited time interval of the DFT simulations (15–20 ps), we found that the correlation converges rather poorly so that a definite conclusion regarding the different contributions is out of reach, except the general conclusion that for all investigated compositions and liquid temperatures, the cross-AF are very small when compared to the self-AF. In addition, the small system size and the short timescale of DFT simulations do not permit linking the detail of atomic trajectories, and possible correlated directions of successive jumps with deviation of the NE relation, embedded in the Haven ratio defined by

$$H_R = 1 + \frac{\int_0^\infty \sum_{i,j,i\neq j} z_i z_j \langle \mathbf{v}_j(0) \cdot \mathbf{v}_i(t) \rangle \mathrm{d}t}{\int_0^\infty \sum_i z_i^2 \langle \mathbf{v}_i(0) \cdot \mathbf{v}_i(t) \rangle \mathrm{d}t} \tag{15}$$

In the present case, we could hardly estimate a meaningful H_R. We note, indeed, that for example, the 900 K isotherm the current cross-correlation is substantially smaller, and fluctuating around a slope near 0. This suggests a very low contribution to overall σ, at least in the liquid state. For this reason, and owing to the poor statistics obtained for the cross-correlations, in the present paper we only consider the autocorrelations. Corresponding data for $\sigma(T)$ [Eq. (12)] are represented in Fig. 10(a) in the liquid state where the simulated liquids can be safely equilibrated. At lower temperatures (glassy state), which are not accessible for dynamic studies from DFT, one usually observes $H_R < 1$ indicative of negative correlations with ions hindering each other's motion. For the 56Na$_2$S-44SiS$_2$ glass, it was found experimentally [72] $H_R = 0.28$.

As for the diffusivity, we find that the calculated conductivities in the melt are in line with those determined in the glassy state at low temperature ($10^3/T > 3.0$) for NS, N5S3, and N2S, since the trends of the low- (experimental) and high-temperature (theoretical) data can eventually connect together close to T_g. Here, one should, however, keep in mind that

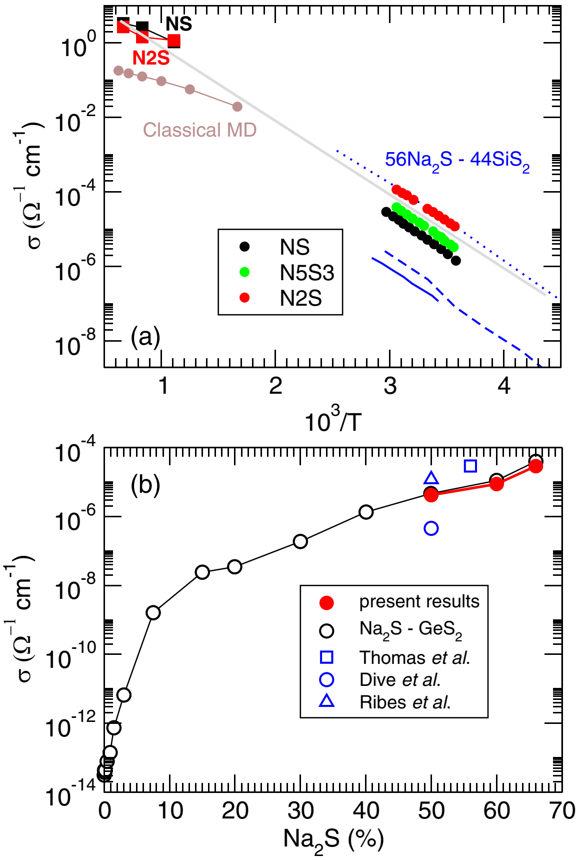

FIG. 10. (a) Calculated conductivities in NS (black-filled squares) and N2S (red-filled squares) melts, compared to classical MD simulations [71] (brown circles), and to experimental measurements in the glassy state (colored circles, present study) and to previously published data of the literature on NS: blue-solid line (Ribes *et al.* [78]), blue-broken line (Dive *et al.* [17]), together with a measurement on 56 Na_2S-44 SiS_2 (blue-dotted line, Thomas *et al.* [72]). Note that because of the use [71] of effective charges and $z_{\rm Na} = 0.6e$, conductivities from classical MD are smaller, although diffusivities (Fig. 9) are higher than the present DFT simulations. (b) Measured room-temperature conductivities as a function of Na_2S content (red), compared to other measurements [17,72,78] and to a parent system [35] (Na_2S-GeS_2, open-black circles).

conductivity jumps or anomalies can occur as the system softens in the glass transition region, and sometimes lead to so-called Arrhenius crossovers [79,80]. These simply signal that with growing temperature, the ion motion becomes increasingly influenced by the motion of the network atoms, which also results in a reduction of viscosity at $T \geqslant T_g$.

We, furthermore, note that $\sigma(T)$ is found to be larger than the values determined at similar temperatures from a classical force-field [71]. All display a possible Arrhenius behavior whose calculated activation energies are found to be of about $E_A = 0.19$–0.20 eV for both compositions. These are somewhat smaller than those determined from the experimental data as we found $E_A = 0.41(1)$ eV, 0.41(3) eV, and 0.37 eV for NS, N3S5, and N2S, respectively. This is consistent with the fact that in the supercooled state, activation barriers are reduced and this enhances the migration of the Na^+ cation through the network. Such cooperative conduction mechanism is sometimes proposed [80–82] to be fitted by a phenomenological Vogel-Fulcher-Tammann law of the form $\ln\sigma \propto A/(T - T_0)$. Here, we can hardly comment more on this given the reduced number of numerical data points. Finally, the calculated activation energies are also smaller than the corresponding calculated values for the isochemical Ge compounds N2G (0.31 eV [35]).

The detail of conductivity contributions can be obtained by splitting Eq. (12) into Nernst-Einstein contributions arising from the Na ions, and from the network species (N), i.e., one focuses on different contributions σ_k ($k =$ Na, N) using

$$\sigma_{\rm Na} = \frac{e^2}{Vk_BT} z_{\rm Na}^2 D_{\rm Na}(T),$$
$$\sigma_N = \frac{e^2}{Vk_BT}\big(z_{\rm S}^2 D_{\rm S}(T) + z_{\rm Si}^2 D_{\rm Si}(T)\big), \tag{16}$$

where D_k is the self-diffusion constant of the species k. In NS melts, the calculated conductivity results mainly from the network atoms (Si,S), which contribute to about 75% of the total conductivity, this being independent of temperature. Conversely, for the N2S system we find a ratio $\sigma_N/\sigma = 0.45$–0.50 at elevated temperature, followed by an increase up to 0.60 at 900 K. The reduction not only results from the reduced statistical contribution of the network species at large modifier content, but also arises at high temperature from a reduction of the diffusivities $D_{\rm Si}$ and $D_{\rm S}$ (Fig. 9). When these features are compared to corresponding lithium based systems, we essentially remark that the diffusivity difference between ion and network species (of about a factor larger than 10) in the latter leads to a dominant contribution of the alkali ion to conductivity in Li-based glasses [67,83]. This is at variance with the present Na-based glasses in which the reduced diffusivity difference (Fig. 9) leads to a dominant contribution of the Si and S species to the global conductivity. It suggests that for sodium thiosilicates and related compounds, the role of the network properties and the way it is altered by, e.g., depolymerization are crucial for the search of conductivity enhancement.

B. From experiments

In Fig. 10(b), we represent the measured room-temperature conductivities σ of the three investigated systems NS, N3S5, and N2S. At room temperature, we do find the largest σ for the N2S glass, which is found to be equal to $2.9 \times 10^{-5}\ \Omega^{-1}\,{\rm cm}^{-1}$. We are not aware of any other measurements at these elevated Na compositions, and this might be because of the fact that previously studied samples were essentially obtained from a melt-quenching technique, which limits the glass-forming range to about 60% Na_2S [6,7]. For the NS glass, the present results ($\sigma = 4.2 \times 10^{-6}\ \Omega^{-1}\,{\rm cm}^{-1}$) are somewhat larger than the experimental results of Dive *et al.* [17] ($4.52 \times 10^{-7}\ \Omega^{-1}\,{\rm cm}^{-1}$) but very close to the one determined by Ribes *et al.* [78] ($1.20 \times 10^{-5}\ \Omega^{-1}\,{\rm cm}^{-1}$). The differences might essentially arise from a different sample preparation procedure (melt quench versus ball milling) and from the molding pressure applied to the cells prior to conductivity measurement, which is known to modify the measured conductivities [84,85].

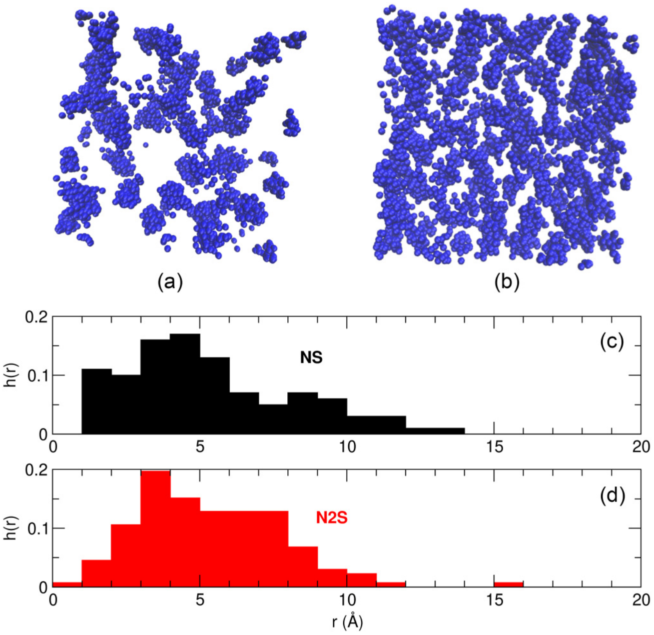

FIG. 11. Atomic snapshot of a slab (5-Å thickness) of liquid (900 K) NS (a) and N2S (b) representing the accumulated trajectories (20 ps) of Na ions. alone. Empty regions correspond to the (Si,S) network. Here, the positions of all sodium ions in the slab at various times $t \leqslant 20$ ps are given with a frame rate of 1 ps. Corresponding normalized distribution $h(r)$ of atomic displacements in NS (c) and N2S (d).

Interestingly, once the same sample preparation and measurement techniques are employed, we note that the conductivity trend at elevated modifier content in Na$_2$S-SiS_2 is very close to the one measured [35] for the isochemical GeS$_2$-Na$_2$S glass, i.e., we found for the latter system for 66% modifier (N2G) a conductivity at room temperature of (6.93×10^{-5} Ω^{-1} cm^{-1}), which is of the same order as the one measured for the present N2S glass. This indicates that the effect of the underlying network structure is similar, and the results from a identical DFT scheme [35] have revealed that both Na-modified Ge- and Si-sulfides share the same structural properties with similar densities: tetrahedral character, presence of edge-sharing tetrahedra that have vanished in the 66% glass, similar Q^n speciation, presence of homopolar defects, etc.

C. Insight into the atomic scale dynamics

1. *Emergence of a spatially unconstrained Na motion*

Using the atomic trajectories, we attempt to sketch the typical dynamics of such fast-ion electrolytes by focusing essentially on the Na motion, and at a temperature (900 K $\simeq 1.6T_g$) at which a "reasonable" trajectory can be considered without influence of the dynamical slowing down because of the onset of glassy relaxation. The network depolymerization obviously impacts the localization of the motion, and this can be qualitatively inferred from a visual inspection of the atomic snapshots [Figs. 11(a) and 11(b)]. Here, one acknowledges for the NS liquid a clear heterogeneous distribution of Na atoms representing a disconnected network of pockets and channels, which is spatially constrained by the presence of a partially remaining (Si,S) network. These features are rather similar to documented archetypal silicates [62,86] but can lead to a spatial extent for the motion that leads to a rather broad distribution $h(r)$ of atomic displacements (0–15 Å) at a fixed simulation time [Fig. 11(c)]. Upon modifier increase and further network depolymerization, the Na motion almost extends to the entire simulation box [Fig. 11(b)], except in reduced places occupied by the isolated Q^0 tetrahedra. As a result, the corresponding atomic displacements are now unconstrained and, in contrast to NS [Fig. 11(c)], lead to a nearly Gaussian-like distribution centered at about 5 Å [Fig. 11(d)]. It is the signature that in highly depolymerized networks, the ion paths result from series of independent random segments as for Brownian motion, which underscores the stochastic nature of the Na motion in N2S, at variance with the one encountered in NS liquids.

2. *Categorizing ion motion*

Recently, typical ion motions have been identified [87] from MD trajectories on a similar compound (2Li$_2$S-GeS$_2$). These can be cast into select categories on the picosecond timescale: reduced cage-like motion in pockets constrained by the surrounding network species, back-and-forth jump motions with short transition states and long-range filamentary motions. These generic classes can be sketched on the timescale of the simulation ($\simeq$20 ps) from the inspection of the individual msds.

Pocket ions (PIONS) are revealed from spatially limited motions typical of a cage-like dynamics or vibrations [black curve, Fig. 12(b)] that is constrained by the surrounding network-forming species or by Na ions, with a cage size of about $\simeq$7 Å. Other Na ions experience jumps over small distances to a neighboring NBS anionic site before eventually moving back to the initial (or close) NBS site, which leads to a msd value close to zero at long times [red curve, Fig. 12(b)]. This back-and-forth motion defines a second category of Na atoms termed back-and-forth ions (BAFIONS). The spatial extent is typically of about 7.0–8.0 Å [plateau value of the red curve in Fig. 12(b)]. Finally, a third category of Na motion is of filamentary nature (FIONS) with a possible limited time ($\simeq$6 ps) spent in trapping sites [blue curve, Fig. 12(b)] separated by substantial spatial jumps, which lead to rather important mean-square displacements (220–250 Å^2 at the largest considered time). We, furthermore, detect that the motion of FIONS might be qualitatively different in NS and N2S liquids. In the former, we have detected that the presence of a residual network leads to a so-called channel dynamics [Fig. 11(a)], and this apparently induces for the Na atoms a rather straight jump between trapping sites as the signature of spatially guided dynamics [Fig. 12(a)]. Conversely, because of the increased number of ions and the complete depolymerization of the network, the same kind of motion in N2S seems to involve some transition state and lead to a pseudo-filamentary motion [Fig. 12(c)].

These features and the fact that one has a distribution of msds indicate that the Na dynamics is heterogeneous in character.

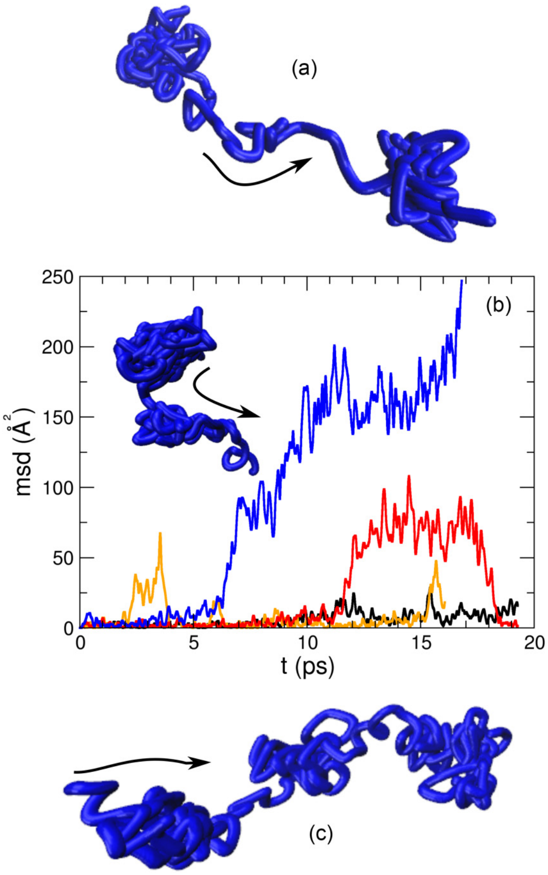

FIG. 12. (a) Typical filamentary single Na motion during 15–20 ps in liquid NS. (b) Mean square displacement of three select Na ions in 900 K NS liquids : pocket motion (black, PIONS), back and forth motion (red and orange, BAFIONS), filamentary motion (blue, FIONS). The snapshot represents a typical BAFION motion. (c) Typical pseudo-filamentary motion in liquid N2S. The arrows indicate the direction of the Na motion.

While such ion motion analysis is rather recent in modified sulfide glasses, a large number of simulation studies [62,88–90] on corresponding oxides (e.g., sodium silicates) have emphasized the variety of ion trajectories: immobile ions trapped in cages, backward jumps, and long-range motion. These are in line with what we detect in the Na_2S-SiS_2 liquid. The fraction of immobile particles can be evaluated from a simple criterion using, e.g., msd $\leqslant 20$ Å^2, the latter value corresponding to the minimum of the pair-correlation $g_{\rm NaNa}(r)$ function, and roughly to the limit of a minimal hopping distance. All particles not fulfilling the condition can be considered as immobile, the statistics being weakly sensitive to this criterion as exemplified from the pocket motion in Fig. 12(b) (black curve), which is radically different from the other types of motion. Using this criterion, we evaluate that 45% Na atoms are immobile in NS (39% in N2S) at 900 K during the MD trajectory.

In sodium silicates, Cormack and coworkers [89,90], furthermore, argue that BAFIONS (i.e., backwards moving ions) are not numerous in glasses given that the lack of long-range order induces a lack of constraints on the local environment of the alkali ions, which makes the original site look different to the ion in its new site and so the propensity to return is reduced. In order to identify such ions [i.e., red and orange curves in Fig. 12(b)], we use the obvious condition msd$(t_0)\simeq 0$ with t_0 equal or less to the maximum simulation time, together with the condition msd$\simeq$cst during a fixed time interval Δt (e.g., orange or red curves in Fig. 12), to identify such backwards moving or BAFIONS. We find that only 15% Na atoms are involved in such kind of motion in NS (20% in N2S).

VI. SUMMARY AND CONCLUSIONS

Here, we have investigated theoretically and experimentally the structural, dynamic, and electrical properties of different compositions in the Na_2S-SiS_2 system, which is an attractive material for applications for all solid state batteries, while also representing a challenging material in terms of atomic scale description. In contrast to their oxide counterparts, sodium silicates, which have received huge attention because of their presence in Earth sciences and their use in a number of industrial and domestic applications, sodium thiosilicates have received only limited attention owing, in part, to their rather important crystallization tendency during melt-quench preparation. As a result, the number of studies is rather limited and traces back to the 1990s [7,78]. However, the increasing demand for batteries using cheap and available raw materials has brought renewed attention to such glasses, since the design of new families of solid electrolytes will need to reconsider the question of the global lithium resources and their associated sustainability issues. In this respect, it is tempting to imagine such sodium thiosilicates being associated with other network-forming compounds (e.g., P_2S_5) or additives (NaCl) in order to boost the conductivity level.

The addition of Na_2S into the base SiS_2 glass induces various structural changes that have been characterized by a combination of x-ray scattering, first principles molecular dynamics, and electric measurements. Results indicate a deep network modification already present at 50% (NS) and even more at 66% (N2S) added Na_2S. Both are dominated by the tetrahedral character of silicon, as in corresponding oxides, but display a network topology that is dramatically different, as edge-sharing connections are possible in chalcogenides, and are obtained successfully from simulation. The addition of Na_2S reveals the disruption of the base network and the progressive disappearance of ES structures. The tetrahedral character of Si atoms remains unchanged, and a Q^n speciation similar to that of corresponding oxides or thiosilicates is obtained. The generic evolution from a Q^4 network (SiS_2) to a nearly Q^0 network ($SiS_4^{4\ominus}$ molecules) is obtained, and the presence of homopolar Si–Si bonds is acknowledged.

Experimental conductivity results indicate that sodium thiosilicate glasses display conductivity levels up to $2.9 \times 10^{-5}\ \Omega^{-1}\,\mathrm{cm}^{-1}$, which are similar to other sulfide glasses, somewhat smaller than their lithium counterparts [91], and very close to conductivities of the isochemical Ge system, which underscores a similar network depolymerization and structure. With temperature, the conductivities display an Arrhenius behavior and might eventually extrapolate to the values calculated in the liquid state from the molecular dynamics simulations, although anomalies might be expected in the glass transition region. As a final comment, we emphasize that these results might help in decoding other glasses of the same family (e.g., alkaline-earth or potassium thiosilicates). They might also help to understand more complex glassy electrolytes using mixed-modifier or network-former systems, both from the experimental and theoretical viewpoint, such as the popular $Li_{10}GeP_2S_{12}$.

ACKNOWLEDGMENTS

This work is supported by Fondation MAIF pour la recherche, and received funding from the European Research Council (ERC) under the European Union's Horizon 2020 research and innovation program (Grant Agreement No. 948780). M.M. acknowledges Chaire d'Excellence between Sorbonne Université and Universidad Autónoma de Mexico (UNAM) for financial support and repeated funding from CNRS and Sorbonne Université. He also acknowledges supercomputing access to the cluster Romeo from Université de Reims Champagne-Ardennes, and has abandoned the idea of being funded by ANR. Ongoing discussions with Gerardo Naumis, Hugo Flores-Ruiz, M. Smedskjaer, and P. Boolchand are gratefully acknowledged.

DATA AVAILABILITY

The data that support the findings of this article are not publicly available because of legal restrictions preventing unrestricted public distribution. The data are available from the authors upon reasonable request.

---

[1] M. Weiss, R. Ruess, J. Kasnatscheew, Y. Levartovsky, N. R. Levy, P. Minnmann, L. Stolz, T. Waldmann, M. Wohlfahrt-Mehrens, D. Aurbach *et al.*, Fast charging of lithium-ion batteries: A review of materials aspects, Adv. Energy Mater. **11**, 2101126 (2021).

[2] K. Bange, H. Jain, and C. Pantano, *Making Glass Better* (International Commission on Glass, Madrid, 2015).

[3] J.-M. Tarascon and M. Armand, Issues and challenges facing rechargeable lithium batteries, Nature (London) **414**, 359 (2001).

[4] C. Masquelier, Lithium ions on the fast track, Nat. Mater. **10**, 649 (2011).

[5] Z. A. Grady, C. J. Wilkinson, C. A. Randall, and J. C. Mauro, Emerging role of non-crystalline electrolytes in solid-state battery research, Front. Energy Res. **8**, 218 (2020).

[6] A. Pradel and A. Piarristeguy, Thio and selenosilicates, sulfide and selenide counterparts of silicates: Similarities and differences, C. R. Géosci. **354**, 79 (2022).

[7] A. Pradel, G. Taillades, M. Ribes, and H. Eckert, ^{29}Si NMR structural studies of ionically conductive silicon chalcogenide glasses and model compounds, J. Non-Cryst. Solids **188**, 75 (1995).

[8] A. Pradel and M. Ribes, Electrical properties of lithium conductive silicon sulfide glasses prepared by twin roller quenching, Solid State Ionics **18–19**, 351 (1986).

[9] J. H. Kennedy, Ionically conductive glasses based on SiS_2, Mater. Chem. Phys. **23**, 29 (1989).

[10] D. Foix, D. Gonbeau, G. Taillades, A. Pradel, and M. Ribes, The structure of ionically conductive chalcogenide glasses: A combined NMR, XPS and *ab initio* calculation study, Solid State Sci. **3**, 235 (2001).

[11] D. Foix, H. Martinez, A. Pradel, M. Ribes, and D. Gonbeau, XPS valence band spectra and theoretical calculations for investigations on thiogermanate and thiosilicate glasses, Chem. Phys. **323**, 606 (2006).

[12] H. Eckert, John H Kennedy, A. Pradel, and M. Ribes, Structural transformation of thiosilicate glasses: ^{29}Si MAS-NMR evidence for edge-sharing in the system Li_2S SiS_2, J. Non-Cryst. Solids **113**, 287 (1989).

[13] S. Kondo, K. Takada, and Y. Yamamura, New lithium ion conductors based on Li_2S-SiS_2 system, Solid State Ionics **53–56**, 1183 (1992).

[14] A. Hayashi, S. Hama, H. Morimoto, M. Tatsumisago, and T. Minami, Preparation of Li_2S–P_2S_5 amorphous solid electrolytes by mechanical milling, J. Am. Ceram. Soc. **84**, 477 (2001).

[15] H. Peng, X. Ma, Z. Fan, and Y. Liang, Preparation structure and properties of the Li_2S-SiS_2 lithium ion conducting glasses, J. Chin. Ceramic Soc. **34**, 1270 (2006).

[16] D. E. Watson and S. W. Martin, Short range order characterization of the $Na_2S + SiS_2$ glass system using Raman, infrared and ^{29}Si magic angle spinning nuclear magnetic resonance spectroscopies, J. Non-Cryst. Solids **471**, 39 (2017).

[17] A. Dive, C. Benmore, M. Wilding, S. W. Martin, S. Beckman, and S. Banerjee, Molecular dynamics modeling of the structure and Na^+-ion transport in $Na_2S + SiS_2$ glassy electrolytes, J. Phys. Chem. B **122**, 7597 (2018).

[18] A. Cade, E. Philippot, M. Ribes, and M. Maurin, Crystal-structure of sodium thiosilicate $Na_4Si_4S_{10}$, C. R. Acad. Sci. C **274**, 1054 (1972).

[19] S. Harm, A.-K. Hatz, C. Schneider, C. Hoefer, C. Hoch, and B. V. Lotsch, Finding the right blend: Interplay between structure and sodium ion conductivity in the system Na_5AlS_4–Na_4SiS_4, Front. Chem. **8**, 90 (2020).

[20] L. F. Gladden and S. R. Elliott, Computer-generated models of a-$SiSe_2$: II. Structural studies, J. Non-Cryst. Solids **109**, 223 (1989).

[21] H. Eckert, Z. Zhang, and J. H. Kennedy, Structural transformation of non-oxide chalcogenide glasses. The short-range order of lithium sulfide (Li_2S)-phosphorus pentasulfide (P_2S_5) glasses studied by quantitative phosphorus-31, lithium-6, and lithium-7 high-resolution solid-state NMR, Chem. Mater. **2**, 273 (1990).

[22] O. Masson, pyTSRedX, a data reduction program to obtain the atomic pair distribution function (PDF) from x-ray total scattering data (2022), http://ftp.esrf.fr/pub/scisoft/xop2.3/dabaxfiles/.

[23] https://ftp.esrf.fr/pub/scisoft/xop2.3/DabaxFiles/

[24] A. K. Soper and P. A. Egelstaff, Multiple scattering and attenuation of neutrons in concentric cylinders: I. Isotropic first scattering, Nucl. Instrum. Methods **178**, 415 (1980).

[25] R. Car and M. Parrinello, Unified approach for molecular dynamics and density-functional theory, Phys. Rev. Lett. **55**, 2471 (1985).

[26] S. Grimme, Accurate description of van der Waals complexes by density functional theory including empirical corrections, J. Comput. Chem. **25**, 1463 (2004).

[27] A. D. Becke, Density-functional thermochemistry. I. The effect of the exchange-only gradient correction, J. Chem. Phys. **96**, 2155 (1992).

[28] C. Lee, W. Yang, and R. G. Parr, Development of the Colle-Salvetti correlation-energy formula into a functional of the electron density, Phys. Rev. B **37**, 785 (1988).

[29] M. Micoulaut, R. Vuilleumier, and C. Massobrio, Improved modeling of liquid GeSe$_2$: Impact of the exchange-correlation functional, Phys. Rev. B **79**, 214205 (2009).

[30] C. Massobrio, M. Micoulaut, and P. S. Salmon, Impact of the exchange-correlation functional on the structure of glassy GeSe$_2$, Solid State Sci. **12**, 199 (2010).

[31] A. Bouzid, C. Massobrio, M. Boero, G. Ori, K. Sykina, and E. Furet, Role of the van der Waals interactions and impact of the exchange-correlation functional in determining the structure of glassy GeTe$_4$, Phys. Rev. B **92**, 134208 (2015).

[32] A. Bouzid, S. Le Roux, G. Ori, M. Boero, and C. Massobrio, Origin of structural analogies and differences between the atomic structures of GeSe$_4$ and GeS$_4$ glasses: A first principles study, J. Chem. Phys. **143**, 034504 (2015).

[33] S. Chakraborty, P. Boolchand, and M. Micoulaut, Structural properties of Ge-S amorphous networks in relationship with rigidity transitions: An *ab initio* molecular dynamics study, Phys. Rev. B **96**, 094205 (2017).

[34] M. Celino, S. Le Roux, G. Ori, B. Coasne, A. Bouzid, M. Boero, and C. Massobrio, First-principles molecular dynamics study of glassy GeS$_2$: Atomic structure and bonding properties, Phys. Rev. B **88**, 174201 (2013).

[35] M. Micoulaut, A. Piarristeguy, O. Masson, L-M Poitras, R. Escalier, A. Kachmar, and A. Pradel, Quantitative assessment of network depolymerization in archetypal superionic glasses and its relationship with ion conduction: A case study on Na$_2$S-GeS$_2$, Phys. Rev. B **108**, 144205 (2023).

[36] M. Micoulaut, Diffraction patterns of amorphous materials as a series expansion of neighbor distribution functions, J. Phys.: Condens. Matter **31**, 285402 (2019).

[37] A. C. Wright, The comparison of molecular dynamics simulations with diffraction experiments, J. Non-Cryst. Solids **159**, 264 (1993).

[38] M. Micoulaut, S. Le Roux, and C. Massobrio, Investigation of size effects on the structure of liquid GeSe$_2$ calculated via first-principles molecular dynamics, J. Chem. Phys. **136**, 224504 (2012).

[39] K. Sykina, E. Furet, B. Bureau, S. Le Roux, and C. Massobrio, Network connectivity and extended Se chains in the atomic structure of glassy GeSe$_4$, Chem. Phys. Lett. **547**, 30 (2012).

[40] G. Ori, A. Bouzid, É. Martin, C. Massobrio, S. L. Roux, and M. Boero, Chalcogenide glasses as a playground for the application of first-principles molecular dynamics to disordered materials, Solid State Sci. **95**, 105925 (2019).

[41] C. Massobrio, A. Pasquarello, and R. Car, Concentration fluctuations on intermediate range distances in liquid GeSe$_2$: The critical role of ionicity, Comput. Mater. Sci. **17**, 115 (2000).

[42] P. L. Silvestrelli, E. Martin, M. Boero, A. Bouzid, G. Ori, and C. Massobrio, Atomic structure of glassy GeTe$_4$ as a playground to assess the performances of density functional schemes accounting for dispersion forces, J. Phys. Chem. B **124**, 11273 (2020).

[43] A. Bouzid, G. Ori, M. Boero, E. Lampin, and C. Massobrio, Atomic-scale structure of the glassy Ge$_2$Sb$_2$Te$_5$ phase change material: A quantitative assessment via first-principles molecular dynamics, Phys. Rev. B **96**, 224204 (2017).

[44] M. Micoulaut, I. Pethes, P. Jóvári, L. Pusztai, M. Krbal, T. Wágner, V. Prokop, Š. Michalik, K. Ikeda, and I. Kaban, Structural properties of chalcogenide glasses and the isocoordination rule: Disentangling effects from chemistry and network topology, Phys. Rev. B **106**, 014206 (2022).

[45] P. S. Salmon, Structure of liquids and glasses in the Ge–Se binary system, J. Non-Cryst. Solids **353**, 2959 (2007).

[46] C. Massobrio, J. Du, M. Bernasconi, and P. S. Salmon, *Molecular Dynamics Simulations of Disordered Materials* (Springer, New York, 2015), Vol. 215.

[47] A. Feltz and G. Pfaff, Über glasbildung und eigenschaften in chalkogenidsystemen; die verbindungen Na$_6$Si$_2$S$_6$ und Na$_6$Si$_2$Se$_6$ und deren bromspaltungsprodukte Na$_3$SiSe$_3$Br und Na$_3$SiSe$_3$Br, Z. Chem. **23**, 68 (1983).

[48] A. Feltz and G. Pfaff, Zur bindungsenergie der Si–Si und Ge–Ge bindung in den verbindungen Na$_6$Si$_2$X$_6$ und Na$_6$Ge$_2$X$_6$ (X = S, Se), Z. Anorganische Allgem. Chem. **504**, 173 (1983).

[49] C. Bischoff, K. Schuller, M. Haynes, and S. W. Martin, Structural investigations of yNa$_2$S+(1- y)PS$_{5/2}$ glasses using Raman and infrared spectroscopies, J. Non-Cryst. Solids **358**, 3216 (2012).

[50] F. Mizuno, A. Hayashi, K. Tadanaga, and M. Tatsumisago, New, highly ion-conductive crystals precipitated from Li$_2$S–P$_2$S$_5$ glasses, Adv. Mater. **17**, 918 (2005).

[51] K. Ohara, A. Mitsui, M. Mori, Y. Onodera, S. Shiotani, Y. Koyama, Y. Orikasa, M. Murakami, K. Shimoda, K. Mori *et al.*, Structural and electronic features of binary Li$_2$S-P$_2$S$_5$ glasses, Sci. Rep. **6**, 21302 (2016).

[52] M. Kassem, T. Bounazef, D. Fontanari, A. Sokolov, M. Bokova, A. C. Hannon, and E. Bychkov, Chemical and structural variety in sodium thioarsenate glasses studied by neutron diffraction and supported by first-principles simulations, Inorg. Chem. **59**, 16410 (2020).

[53] J. Du and A. N. Cormack, The medium range structure of sodium silicate glasses: A molecular dynamics simulation, J. Non-Cryst. Solids **349**, 66 (2004).

[54] X. Yuan and A. N. Cormack, Local structures of MD-modeled vitreous silica and sodium silicate glasses, J. Non-Cryst. Solids **283**, 69 (2001).

[55] D. Cabaret, F. Mauri, and G. S. Henderson, Oxygen k-edge xanes of germanates investigated using first-principles calculations, Phys. Rev. B **75**, 184205 (2007).

[56] M. Micoulaut, M-V Coulet, A. Piarristeguy, M. R. Johnson, Gabriel J Cuello, C. Bichara, J-Y Raty, H. Flores-Ruiz, and A. Pradel, Effect of concentration in Ge-Te liquids: A combined density functional and neutron scattering study, Phys. Rev. B **89**, 174205 (2014).

[57] M. Ribes, J. Olivier-Fourcade, E. Philippot, and M. Maurin, Etude structurale de thiocomposés à groupement anionique de type tétrane Na$_4$X$_4$S$_{10}$ (X = Ge, Gi) et Ba$_2$Ge$_4$S$_{10}$, J. Solid State Chem. **8**, 195 (1973).

[58] J.-Y. Raty, C. Otjacques, J.-P. Gaspard, and C. Bichara, Amorphous structure and electronic properties of the Ge$_1$Sb$_2$Te$_4$ phase change material, Solid State Sci. **12**, 193 (2010).

[59] H. Flores-Ruiz and M. Micoulaut, Crucial role of S$_8$-rings in structural, relaxation, vibrational, and electronic properties of liquid sulfur close to the λ transition, J. Chem. Phys. **157**, 054507 (2022).

[60] Q. Zhou, T. Du, L. Guo, M. M. Smedskjaer, and M. Bauchy, New insights into the structure of sodium silicate glasses by force-enhanced atomic refinement, J. Non-Cryst. Solids **536**, 120006 (2020).

[61] H. W. Nesbitt, G. S. Henderson, G. M. Bancroft, and R. Ho, Experimental evidence for na coordination to bridging oxygen in Na-silicate glasses: Implications for spectroscopic studies and for the modified random network model, J. Non-Cryst. Solids **409**, 139 (2015).

[62] P. Jund, W. Kob, and R. Jullien, Channel diffusion of sodium in a silicate glass, Phys. Rev. B **64**, 134303 (2001).

[63] A. Meyer, J. Horbach, W. Kob, F. Kargl, and H. Schober, Channel formation and intermediate range order in sodium silicate melts and glasses, Phys. Rev. Lett. **93**, 027801 (2004).

[64] A. Meyer, F. Kargl, and J. Horbach, Channel diffusion in sodium silicate melts, Neutron News **23**, 35 (2012).

[65] M. Micoulaut and P. Boolchand, Signature of coordination defects in the vibrational spectrum of amorphous chalcogenides, Front. Mater. **6**, 283 (2019).

[66] A. S. Tverjanovich, O. B. Tsiok, V. V. Brazhkin, M. Bokova, A. Cuisset, and E. Bychkov, Remarkably stable glassy GeS_2 densified at 8.3 GPa: Hidden polyamorphism, contrasting optical properties, Raman and DFT studies, and advanced applications, J. Phys. Chem. B **127**, 9850 (2023).

[67] L.-M. Poitras and M. Micoulaut, Establishement of an empirical force-field for crystalline and amorphous Li_2S–SiS_2 electrolytes, Phys. Rev. B **107**, 214205 (2023).

[68] M. Micoulaut and R. Kerner, The structure of lithium silicon sulphide glass systems, J. Phys.: Condens. Matter **9**, 2551 (1997).

[69] H. Maekawa, T. Maekawa, K. Kawamura, and T. Yokokawa, The structural groups of alkali silicate glasses determined from ^{29}Si MAS-NMR, J. Non-Cryst. Solids **127**, 53 (1991).

[70] L. Deng and J. Du, Effects of system size and cooling rate on the structure and properties of sodium borosilicate glasses from molecular dynamics simulations, J. Chem. Phys. **148**, 024504 (2018).

[71] S. S. Sørensen, M. M. Smedskjaer, and M. Micoulaut, Evidence for complex dynamics in glassy fast ion conductors: The case of sodium thiosilicates, J. Phys. Chem. B **127**, 10179 (2023).

[72] M. P. Thomas, N. Lee Peterson, and E. Hutchinson, Tracer diffusion and electrical conductivity in sodium-rubidium silicon sulfide glasses, J. Am. Ceram. Soc. **68**, 99 (1985).

[73] I. Alekseev, D. Fontanari, A. Sokolov, M. Bokova, M. Kassem, and E. Bychkov, *Ionic Conductivity and Tracer Diffusion in Glassy Chalcogenides* (World Scientific, Singapore, 2020), Vol. 1.

[74] E. Bychkov, Tracer diffusion studies of ion-conducting chalcogenide glasses, Solid State Ionics **136–137**, 1111 (2000).

[75] M. Bauchy, B. Guillot, M. Micoulaut, and N. Sator, Viscosity and viscosity anomalies of model silicates and magmas: A numerical investigation, Chem. Geol. **346**, 47 (2013).

[76] J.-P. Hansen and I. R. McDonald, *Theory of Simple Liquids: With Applications to Soft Matter* (Academic Press, New York, 2013).

[77] P. Kubisiak and A. Eilmes, Estimates of electrical conductivity from molecular dynamics simulations: How to invest the computational effort, J. Phys. Chem. B **124**, 9680 (2020).

[78] M. Ribes, B. Barrau, and J. L. Souquet, Sulfide glasses: Glass forming region, structure and ionic conduction of glasses in $Na_2S\,XS_2$ ($X = Si$; Ge), $Na_2S\ P_2S_5$ and $Li_2S\ GeS_2$ systems, J. Non-Cryst. Solids **38–39**, 271 (1980).

[79] M. Malki, V. Magnien, O. Pinet, and P. Richet, Electrical conductivity of iron-bearing silicate glasses and melts. Implications for the mechanisms of iron redox reactions, Geochim. Cosmochim. Acta **165**, 137 (2015).

[80] M. Malki and P. Echegut, Electrical conductivity of the CaO–SiO_2 system in the solid and the molten states, J. Non-Cryst. Solids **323**, 131 (2003).

[81] H. Fan, L. Del Campo, V. Montouillout, and M. Malki, Ionic conductivity and boron anomaly in binary lithium borate melts, J. Non-Cryst. Solids **543**, 120160 (2020).

[82] J. L. Souquet, M. Duclot, and M. Levy, Ionic transport mechanisms in oxide based glasses in the supercooled and glassy states, Solid State Ionics **105**, 237 (1998).

[83] M. Micoulaut, L-M Poitras, S. S. Sørensen, H. Flores-Ruiz, and G. G. Naumis, Compressibility, diffusivity, and elasticity in relationship with ionic conduction: An atomic scale description of densified Li_2S-SiS_2, J. Am. Ceramic Soc. **107**, 7711 (2024).

[84] A. Sakuda, A. Hayashi, and M. Tatsumisago, Sulfide solid electrolyte with favorable mechanical property for all-solid-state lithium battery, Sci. Rep. **3**, 2261 (2013).

[85] M. So, G. Inoue, R. Hirate, K. Nunoshita, S. Ishikawa, and Y. Tsuge, Effect of mold pressure on compaction and ion conductivity of all-solid-state batteries revealed by the discrete element method, J. Power Sources **508**, 230344 (2021).

[86] M. Bauchy and M. Micoulaut, From pockets to channels: Density-controlled diffusion in sodium silicates, Phys. Rev. B **83**, 184118 (2011).

[87] M. Micoulaut, Pockets, jumps and filaments: Classifying ionic motion and determining the role of structure in electrochemical properties of $2Li_2S$-GeS_2 superionic glasses, J. Phys.: Condens. Matter **36**, 195703 (2024).

[88] N. T. Thao, N. V. Yen, and P. T. Lien, Diffusion behaviors of sodium atoms within Si–O network in sodium silicate glasses: Insights from molecular dynamics simulations, Eur. Phys. J. B **96**, 138 (2023).

[89] A. N. Cormack, J. Du, and T. R. Zeitler, Sodium ion migration mechanisms in silicate glasses probed by molecular dynamics simulations, J. Non-Cryst. Solids **323**, 147 (2003).

[90] A. N. Cormack, J. Du, and T. R. Zeitler, Alkali ion migration mechanisms in silicate glasses probed by molecular dynamics simulations, Phys. Chem. Chem. Phys. **4**, 3193 (2002).

[91] J. L. Souquet, E. Robinel, B. Barrau, and M. Ribes, Glass formation and ionic conduction in the $M_2S\ GeS_2$ ($M = Li$, Na, Ag) systems, Solid State Ionics **3–4**, 317 (1981).